ELECTROCHEMISTRY

Polysulfonated covalent organic framework as active electrode host for mobile cation guests in electrochemical soft actuator

Manmatha Mahato[1], Mousumi Garai[1], Van Hiep Nguyen[1], Saewoong Oh[1], Sanghee Nam[1], Xiangrong Zeng[1], Hyunjoon Yoo[1], Rassoul Tabassian[1,2]*, Il-Kwon Oh[1]*

Tailoring transfer dynamics of mobile cations across solid-state electrolyte-electrode interfaces is crucial for high-performance electrochemical soft actuators. In general, actuation performance is directly proportional to the affinity of cations and anions in the electrolyte for the opposite electrode surfaces under an applied field. Herein, to maximize electrochemical actuation, we report an electronically conjugated *polysulfonated* covalent organic framework (*p*S-COF) used as a common electrolyte-electrode host for 1-ethyl-3-methylimidazolium cation embedded into a Nafion membrane. The *p*S-COF–based electrochemical actuator exhibits remarkable bending deflection at near-zero voltage (~0.01 V) and previously unattainable blocking force, which is 34 times higher than its own weight. The ultrafast step response shows a very short rising time of 1.59 seconds without back-relaxation, and substantial ultralow-voltage actuation at higher frequencies up to 5.0 hertz demonstrates good application prospects of common electrolyte-electrode hosts. A soft fluidic switch is constructed using the proposed soft actuator as a potential engineering application.

INTRODUCTION

In electrochemical systems, specifically in electrical double-layer capacitors (EDLCs), the transformation of electrical energy into chemical energy is driven by the migration of electrolyte ions between the opposite electrodes (*1–5*). A high cycling efficiency combined with a long cycle life and exceptional manipulability achieved by subtle structural modifications of both electrode and electrolyte render EDLCs suitable for future energy storage devices (*6–10*). Electroionic soft actuators follow the EDLC principle, in which the migration of dissimilar electrolyte ions causes a bending deflection (*11–15*). Recent advances in the development of electronically conjugated carbon materials with good capacitance have demonstrated their potential applicability as active electrode materials for high-performance electrochemical soft actuators owing to adoptable antagonistic surface nanoengineering (*16–20*). The presence of π-conjugated polar functional moieties and large specific surface areas is considered the driving force in interfacial fast ion transfer processes owing to their switchable antagonistic electronic conductive path and ionic charge capacitance properties (*21–23*). It was shown that small changes in surface functionality can substantially alter the electrochemical properties of the active materials. However, developing a surface-functionalized active electrode material with desired characteristics and optimizing electrochemical actuation under ultralow voltages remain challenging tasks.

Abundant tailorable functionalities of covalent organic frameworks (COFs) have emerged to modulate the surface properties for designing active electrodes and/or electrolyte materials suitable for ultrastable electrochemical single-ion conduction (*24–26*). In addition, COFs generally contain electrolyte-accessible pores with large active surfaces for the fast diffusion of electrolyte ions. In a recent work, a π-conjugated crystalline two-dimensional (2D) polyarylimide COF with naphthalene diimide surface functionalities was introduced as an active cathode material for the ultrastable and ultrafast lithium storage (*27*). Sulfonated functional COFs have been developed to overcome the shortcomings of all-solid-state Li-ion and Zn-ion batteries, in which electropositive Li and Zn ions with high densities are transferred via covalently tethered electronegative sulfonate surface moieties (*28–30*). Surface functionalities play a vital role in achieving long-term electrochemical cycle stability and high device performance. The presence of functional sites on the backbones of active materials (electrodes or electrolytes) promotes the reversible electrochemical transport of ions owing to mutual interactions assisted by an external field. The effects of π-conjugation and surface polarity on the properties of a stable and fast electrochemical soft actuator were examined by using a nitrogen-rich and sulfur-rich π-conjugated COF-based electrode containing hydroxyl functional groups (*31*). Here, the electronic conjugation facilitates fast ion movement, while the nanoporous structural surface with high active areas contributes to the accommodation of larger amounts electrolyte ions. However, the utilization of specific surface functional groups for improving the performance of electrochemical soft actuators has not been explored yet. Thus, the possibility of designing surface functional groups as common hosts for both the electrode and electrolyte remains unexplored and can be potentially realized to modulate the output of an electrochemical device.

Herein, we report an electronically conjugated *polysulfonated* COF (*p*S-COF) for a common electrolyte-electrode host of electrochemical soft actuators. The electronically conjugated *p*S-COF is synthesized as an active electrode material to produce common surface sulfonate functionalities and facilitate the relaxing exchange

[1]National Creative Research Initiative for Functionally Antagonistic Nano-Engineering, Department of Mechanical Engineering, Korea Advanced Institute of Science and Technology (KAIST), 291 Daehak-ro, Yuseong-gu, Daejeon 34141, Republic of Korea. [2]Department of Mechanical and Production Engineering, Aarhus University, Katrinebjergvej 89 G-F, 8200 Aarhus N, Denmark.
*Corresponding author. Email: r.tabassian@mpe.au.dk (R.T.); ikoh@kaist.ac.kr (I.-K.O.)

of 1-ethyl-3-methylimidazolium (EMIM$^+$) guest electrolyte cations embedded in Nafion. The structural authenticity and successful synthesis of the designed pS-COF are verified both experimentally and theoretically. The common surface sulfonate moieties of all-solid-state electrolyte-electrodes provide an easy and relaxing platform for the exchange accommodation of movable EMIM$^+$ guest ions in an electrochemical environment. In addition, the electrode surface containing the 3D nanoporous channels of the crystalline pS-COF acts as a nanoreactor for the abundant stress-free movement of ions. Subsequently, a milestone is achieved by shifting the threshold electric stimulus to 0.01 V, which represents a unique architectural feature of the designed pS-COF–based electrochemical soft actuator (pS-COF–PP). The sulfonate groups serving as a common host increase the charge storage and discharge capacity of a poly(3,4-ethylenedioxythiophene)–poly(styrenesulfonate) (PEDOT-PSS or PP) soft actuator with an areal ionic capacitance of 139 mF cm^{-2} by up to a factor of 12. An ultrastable electrochemical cyclic voltammetric response obtained during 100 cycles with a 97.6% cyclic retention after 100 hours of continuous charging and discharging processes confirm the structural advantages of the pS-COF–PP soft actuator for steady and durable actuation. The strategy of using a common sulfonate host has potentially increased both the bending strain difference (ε) and normalized blocking force (κ) of a traditional electrochemical soft actuator. The proposed pS-COF–PP electrochemical soft actuator exhibits a remarkable strain of 0.56% at 0.5 V and 0.83% at 1.0 V, dc, while the normalized blocking force is approximately 34 times greater than its weight at a dc input voltage of 2.0 V. In addition, the relaxing exchange of electrolyte EMIM$^+$ ions observed for the pS-COF–PP soft actuator increases the actuation speed by nearly 19 times by completely overcoming the back-relaxation effects of the PP soft actuator. Last, upgrading the interior properties of the pS-COF–PP soft actuator enables the successful demonstration of a soft fluidic switch that can effectively control the flow of fluids in a confined channel.

RESULTS

Synthesis and structural characterization of pS-COF active electrode material

To graft sulfonate functional groups onto the active electrode surface, we thoroughly mixed 4,4′-diamino-2,2′-stilbenedisulfonic acid (DSA) and 1,3,5-triformylphloroglucinol (TP) inside a vacuum-sealed glass ampoule before a solvothermal treatment (see Materials and Methods for details). The obtained electronically conjugated and crystalline nanoporous pS-COF was used to fabricate a soft-touch fluidic switch operating at ultralow voltages (Fig. 1). Figure 1A illustrates the synthesis of polycrystalline pS-COFs with plausible chemical structures and shows the refined powder x-ray diffraction (PXRD) patterns obtained both experimentally and theoretically (fig. S1, A and B; for details, see the Supplementary Materials). Figure S1 (C and D) shows the theoretically modeled unit cell, crystal lattice, and interlayer structural configurations obtained for the eclipsed and staggered pS-COF orientations, respectively. The structural parameters of both configurations are listed in table S1. It is worth noting that pS-COFs have structural isomers, imine and keto, due to tautomeric stability as shown in fig. S2. Figure 1B schematically describes the ultralow-voltage–driven bending mechanism and basic configuration of the electroactive soft switch prepared from the as-

synthesized pS-COF serving as an active electrode material (see Materials and Methods for details). A plausible stress-free interaction of the electrode surface with a guest molecule is depicted, where the 3D nanoporous channel of pS-COF serves as a nanoreactor for the accommodation and relaxing exchange of electrolyte ions. Here, the sulfonate moiety acts as a common host for EMIM$^+$ ions from both sides of the all-solid-state pS-COF electrode and the Nafion electrolyte. It can readily interact with the guest ions toward the reversal accommodation of EMIM$^+$ during switching of the electrical signal. The fabricated electroactive soft switch was used to demonstrate the effective control of a fluid flow in a confined channel under an ultralow voltage (Fig. 1C). It is noteworthy that, unlike other actuators, the pS-COF–based soft switch exhibits the highest strain and force with an ultrafast response, which allows effective blockage of the target channel, leading to a unidirectional fluid flow. The superhydrophobic surface of the soft fluidic switch prevents the adhesion of liquid droplets and completely controls the fluid dynamics (Materials and Methods and fig. S3, A to H).

Field-emission scanning electron microscopy (FESEM) and high-resolution transmission electron microscopy (HRTEM) were performed to observe the extremely porous pS-COF surfaces (Fig. 2, A to C, and fig. S4, A to D). The well-defined nanoporous surface morphology (Fig. 2, B and C) facilitates the to-and-from transportation of electrolyte ions during the switching of the electrical signal in the actuator configuration. It can also provide space for accommodating a large number of guest ions within a short period to maximize the electrode deformation and force. The surface characteristics of the synthesized pS-COF (Fig. 1A) are reflected by the elemental mapping images corresponding to the HRTEM high-angle annular dark-field (HAADF) image (Fig. 2, D to I). The structural authenticity of pS-COF was supported by the chronological distribution of building-block elements, which include carbon (Fig. 2E), nitrogen (Fig. 2F), oxygen (Fig. 2G), sulfur (Fig. 2H), and overall carbon-nitrogen-oxygen-sulfur (Fig. 2I). The heteroatom-containing sulfonated functional nanoporous surfaces of pS-COF substantially improve the ion storage capacity of the electrodes in the proposed EDLC-type soft switch.

A type II N$_2$-physisorption isotherm illustrating the microporous and macroporous surface properties of pS-COF indicates that the material exhibits a specific surface area of 167 m^2 g^{-1} (Fig. 3A). The narrow pore size distribution with a pore diameter of 1.27 nm obtained for the pS-COF micropores and wider macroporous structures (pore width, 5 to 70 nm) confirms the unrestricted monolayer-multilayer surface adsorption of guest molecules and/or ions (inset of Fig. 3A). This extremely large electrolyte-accessible active surface enables the instantaneous charging and/or discharging of ions at pS-COF–based electrodes during electrochemical processes and is highly beneficial for the high-frequency and ultrafast actuation. The charging/discharging of electrolyte ions is accelerated by the extended π-electronic conjugation path of the pS-COF active electrode material. The obtained solid-state ultraviolet (UV)–visible absorption spectra confirm the existence of delocalized π-electrons in the pS-COF structure owing to its excellent light absorption properties in the entire visible region (Fig. 3B). The conjugated structural backbones of pS-COF not only enhance the electrochemical conduction processes for faster cyclic charging and/or discharging but also increase the overall ion storage capacity owing to the heteroatom-dominant polar surface (inset of Fig. 3B).
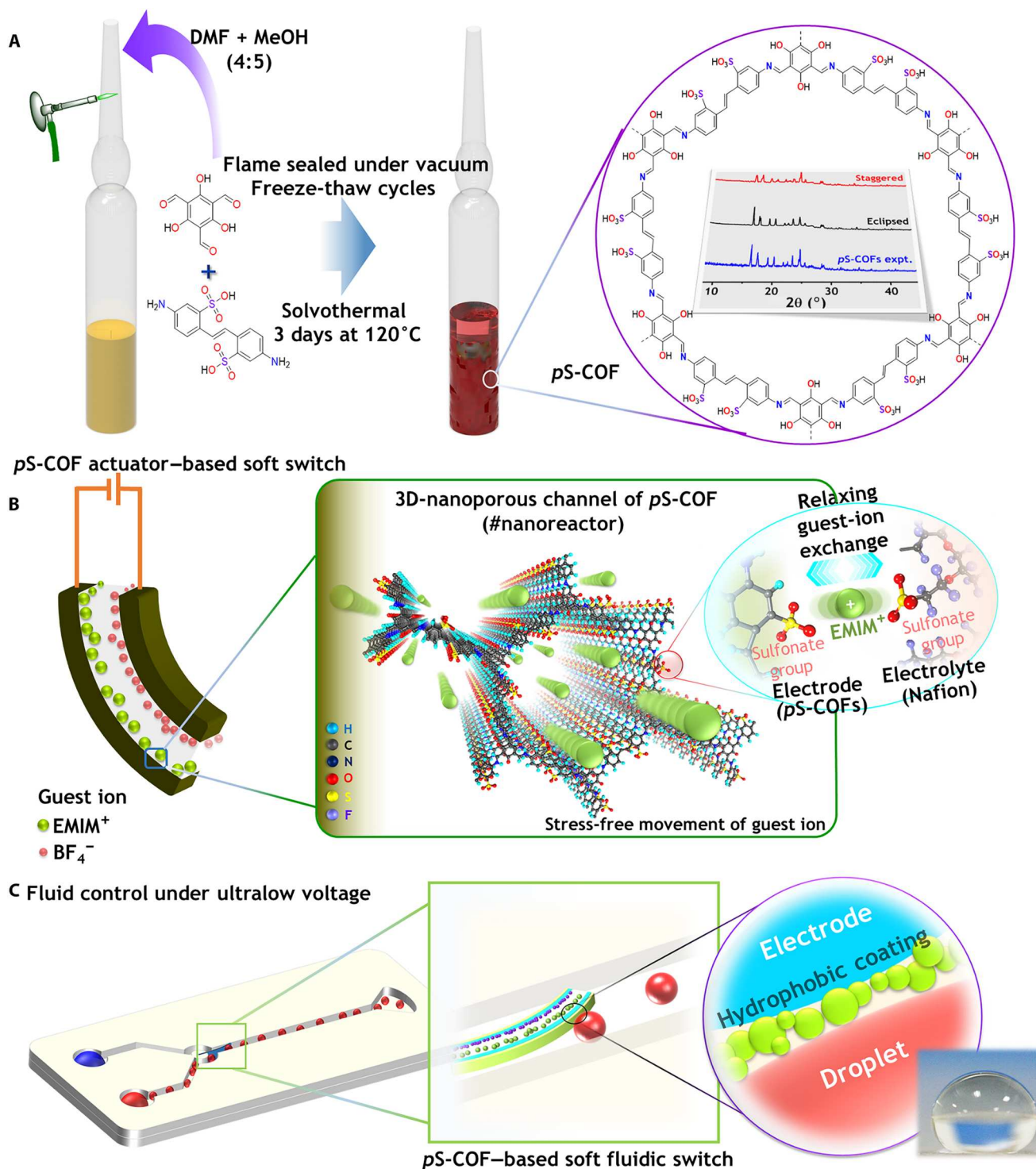
Fig. 1. Synthesis and fundamental use of *p*S-COFs as common electrode-electrolyte host for electroactive soft fluidic switch. (**A**) Schematic illustration for the typical solvothermal synthesis of *p*S-COFs with plausible unit-cell chemical structure and x-ray diffraction patterns. (**B**) Schematic sketch for the working principle of electrochemical soft switch, highlighting the importance of *p*S-COFs for originating common host platform toward relaxed mechanical bending under ultralow electrical field. The accelerated movement of electrolyte ions inside 3D nanoporous channels of *p*S-COFs and relaxing exchange of guest ions by the common sulfonate moieties from both the end of electrode and electrolyte are shown. (**C**) Schematic illustration for the use of *p*S-COFs–based electrochemical soft switch to control the fluids flow under dynamic motion. The superhydrophobic surface of *p*S-COFs–based electrode that can restrict the adhesion of fluid droplets is shown.
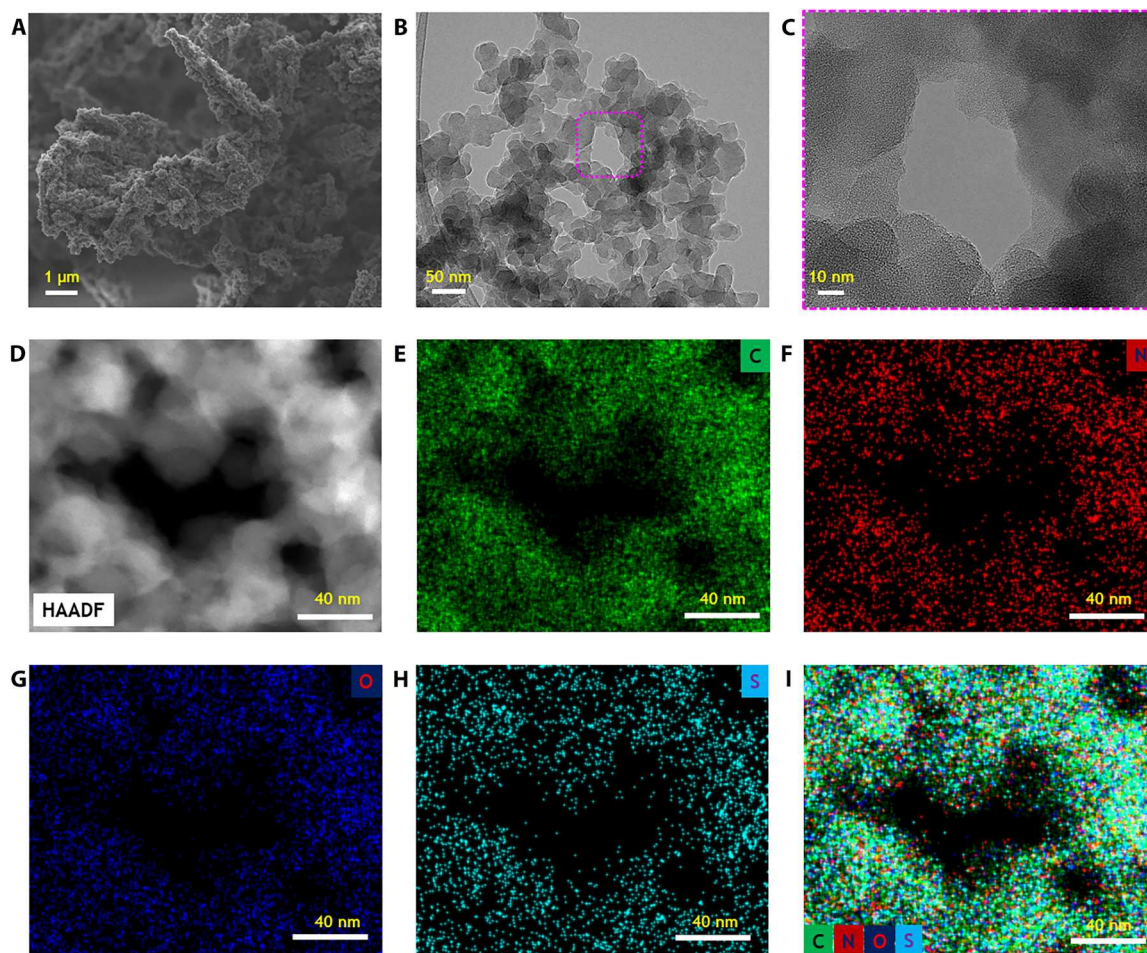
Fig. 2. Nanoporous morphological images and nanoscale structural outlines of *p*S-COFs. (**A**) Field-emission SEM image of *p*S-COFs. Its extremely porous surface structure is shown. (**B** and **C**) High-resolution TEM images of *p*S-COFs with 50- and 10-nm scale bars. Well-defined nanoporous surface morphology with layered configuration is shown. (**D** to **I**) Nanoscale structural and elemental surface outline of *p*S-COFs. (D) HAADF-STEM tomography image of *p*S-COFs. Chronological distribution of building-block elements generated from the tomography image, which include (E) carbon, (F) nitrogen, (G) oxygen, (H) sulfur, and (I) overlapped carbon-nitrogen-oxygen-sulfur. Methodical appearances of anticipated elements throughout the surface are shown.

To verify the structural integrity of *p*S-COF, we have used various spectroscopic techniques (Fig. 3, C to I, and fig. S5, A to C). The successful solvothermal synthesis of *p*S-COF from DSA and TP precursors was initially confirmed by Fourier transform infrared (FTIR) spectroscopy (Fig. 3C). The appearance of a extra FTIR transmittance peak at 1614 cm^{-1} relative to the —C═N stretching mode of *p*S-COF indicates the formation of imine linkages and growth of the framework structure. Simultaneously, the *p*S-COF purity was verified by the complete disappearance of the characteristic —C═O (1636 cm^{-1}) and aromatic —N—H stretching vibrational modes (3141 and 3079 cm^{-1}) previously observed for TP and DSA, respectively. The presence of layered structures and long-range periodicity of *p*S-COF were confirmed by small-angle x-ray scattering (SAXS) and PXRD, respectively (Fig. 3D and the inset of Fig. 3D). The long periodic spacing of the proposed *p*S-COF resulted in a layer thickness (*L*) of 82.7 nm corresponding to the momentum transfer in the reciprocal space (*q*) of 0.076 nm^{-1} (Fig. 3D). This result is similar to the *p*S-COF layer thickness of 83 nm determined from the HRTEM images (fig. S4, C and D). The inset of

Fig. 3D displays the characteristic PXRD peaks of the developed *p*S-COF at 2θ values of 16.23°, 17.36°, 19.15°, 20.20°, 23.40°, and 24.69° corresponding the (001), (201), (221), (440), (800), and (361) planes, respectively. To simulate possible PXRD patterns for both the AA (eclipsed) and AB stacking (staggered) configurations (fig. S1, A and B), the *p*S-COF structure was optimized via 2D modeling using a hexagonal (*P*6/*m*) space group and density functional tight-binding method. The experimental PXRD pattern matched well the results of *p*S-COF conventional modeling in the fully eclipsed AA stacking mode (*R*p, 6.56%; *R*wp, 9.85%) as compared with the staggered AB stacking mode (*R*p, 7.64%; *R*wp, 11.60%). The typical simulated structural parameters of both the eclipsed and staggered *p*S-COF configurations are listed in table S1. The solid-state ^{1}H and ^{13}C cross-polarization magic angle spinning (CP-MAS) nuclear magnetic resonance (NMR) spectra support the presence of *p*S-COF functional groups (Fig. 3E and fig. S5A). The four assigned nonequivalent protons of the *p*S-COF structure (inset of Fig. 3E) generated distinct ^{1}H NMR signals with expected chemical shifts at 14.23, 8.85, 5.38, and 3.27 ppm corresponding to
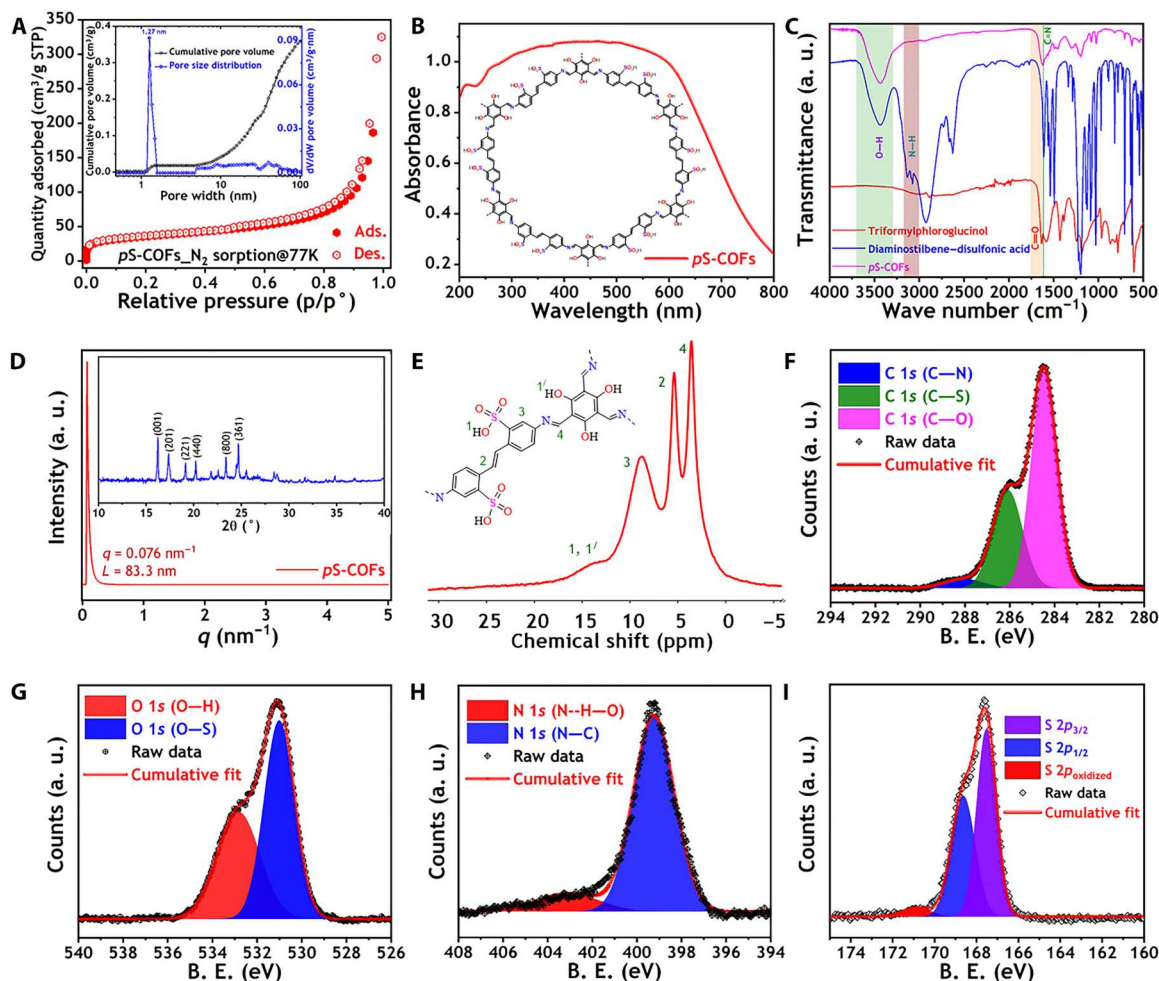
Fig. 3. In-depth physicochemical and structural identification of *p*S-COFs active electrode material. (**A**) N_2 adsorption-desorption isotherm of nanoporous *p*S-COFs at 77 K. Type II physisorption isotherm with Brunauer-Emmett-Teller specific surface area of 167 $m^2\,g^{-1}$. Inset: NLDFT pore size distribution of *p*S-COF electrode material corresponding to N_2-sorption isotherm. (**B**) Solid-state UV-visible (DRS) absorbance spectra of *p*S-COFs active electrode material. (**C**) FTIR spectra of *p*S-COFs and the associated precursors, TP and DSA. The growth of framework structures is shown by presenting the typical transmittance peak for imine linkages at 1614 cm^{-1}. a. u., arbitrary units. (**D**) SAXS pattern of *p*S-COFs electrode material. Inset: Characteristic powder XRD response pattern of *p*S-COFs. Experimentally observed XRD pattern of *p*S-COFs was well matched with the eclipsed AA stacking mode with the *R*p and *R*wp values of 6.56 and 9.85%, respectively. (**E**) Solid-state ^{1}H CP-MAS NMR spectra of *p*S-COFs active material. The spectra confirm the structural integrity by displaying the characteristic NMR signals corresponding to four assigned available nonequivalent protons. (**F**) C 1*s* XPS spectra of *p*S-COFs. Plausible three different carbon configurations after deconvolution are shown as blue: C—N, olive: C—S, and pink: C—O. B. E., binding energy. (**G**) O 1*s* XPS spectra of *p*S-COFs. Two anticipated oxygen configurations are shown as red: O—H and blue: O—S. (**H**) N 1*s* XPS spectra of *p*S-COFs. Both the characteristic imine (blue) and H-bonded (red) nitrogen after deconvolution are shown. (**I**) S 2*p* XPS spectra of *p*S-COFs. The expected atomic configurations of sulfur are shown as purple: S $2p_{3/2}$, blue: S $2p_{1/2}$, and red: $S_{oxidized}$ after deconvolution.

the highly deshielded hydroxylic (denoted as 1 and 1′), deshielded aromatic (denoted as 3), benzylic (denoted as 2), and imine (denoted as 4) protons, respectively (Fig. 3E). In addition, 10 different types of chemically nonequivalent carbons are detected in the ^{13}C CP-MAS NMR spectrum of the *p*S-COF chemical structure (inset of Fig. 3E) with anticipated chemical shifts (fig. S5A). The inset in fig. S5A shows the distinct representation of different carbons in *p*S-COF after deconvolution. Details of the ^{13}C NMR analyses are provided in the Supplementary Materials. To obtain more *p*S-COF structural details, we investigated atomic configurations of its constituent elements via x-ray photoelectron spectroscopy (XPS) (Fig. 3, F to I). Three major distinguishable carbon configurations of *p*S-COF, which contained chemically attached

nitrogen (C—N: blue), sulfur (C—S: olive), and oxygen (C—O: pink) atoms, were identified from the deconvoluted C 1*s* XPS profile with peak binding energies of 288.07, 286.09, and 284.47 eV, respectively (Fig. 3F). It is noteworthy that the XPS peak of the C—C configuration overlapped with the C—O spectrum. The deconvoluted O 1*s* XPS profile exhibits two distinct peaks with binding energies of 532.95 eV (red) and 530.98 eV (blue), which correspond to the O—H and O—S moieties, respectively (Fig. 3G). The N 1*s* XPS profile confirms the presence of nitrogen in the two different *p*S-COF configurations (Fig. 3H). The imine nitrogen, which is bonded to carbon (N—C), produces a strong XPS signal at a binding energy of 399.24 eV. However, the appearance of a broad peak between 406 and 401 eV in the deconvoluted N 1*s*

spectrum suggests the presence of H-bonding interactions (N--H—O) between the imine nitrogen atoms and hydroxyl protons of the adjacent aromatic moieties (*31*). The lone pair electrons of nitrogen atoms can be easily involved in H-bonding interactions through a thermodynamically stable six-membered cyclic transition state with the proton of the hydroxyl group located at the favorable position of an adjacent benzene ring (*32, 33*). This interaction substantially inhibits the keto-enol tautomerization process and facilitates electronic conjugation in an extended *p*S-COF to achieve better electrochemical performance. Figure 3I shows the presence of sulfonated sulfur species in the *p*S-COF structures with expected atomic configurations. The signature S $2p_{3/2}$, S $2p_{1/2}$, and $S_{oxidized}$

peaks of sulfonate moieties are clearly detected in the deconvoluted S $2p$ spectrum at their usual binding energies of 167.53, 168.63, and 170.89 eV, respectively. Furthermore, the XPS survey spectrum (fig. S5B) and elemental analysis data (table S2) confirm the proposed unit-cell chemical structure of *p*S-COF by listing building-block elements with desirable percentages. Moreover, *p*S-COF is thermally stable at temperatures up to 300°C (fig. S5C). Last, to determine the molecular weight of *p*S-COFs, we performed the matrix-assisted laser desorption/ionization−time-of-flight mass analysis using a 2,5-dihydroxybenzoic acid matrix. The *p*S-COFs have a maximum molecular weight of 430655.024, indicating a 139-mer (fig. S6). Chemical stability in both aqueous and nonaqueous solvents,
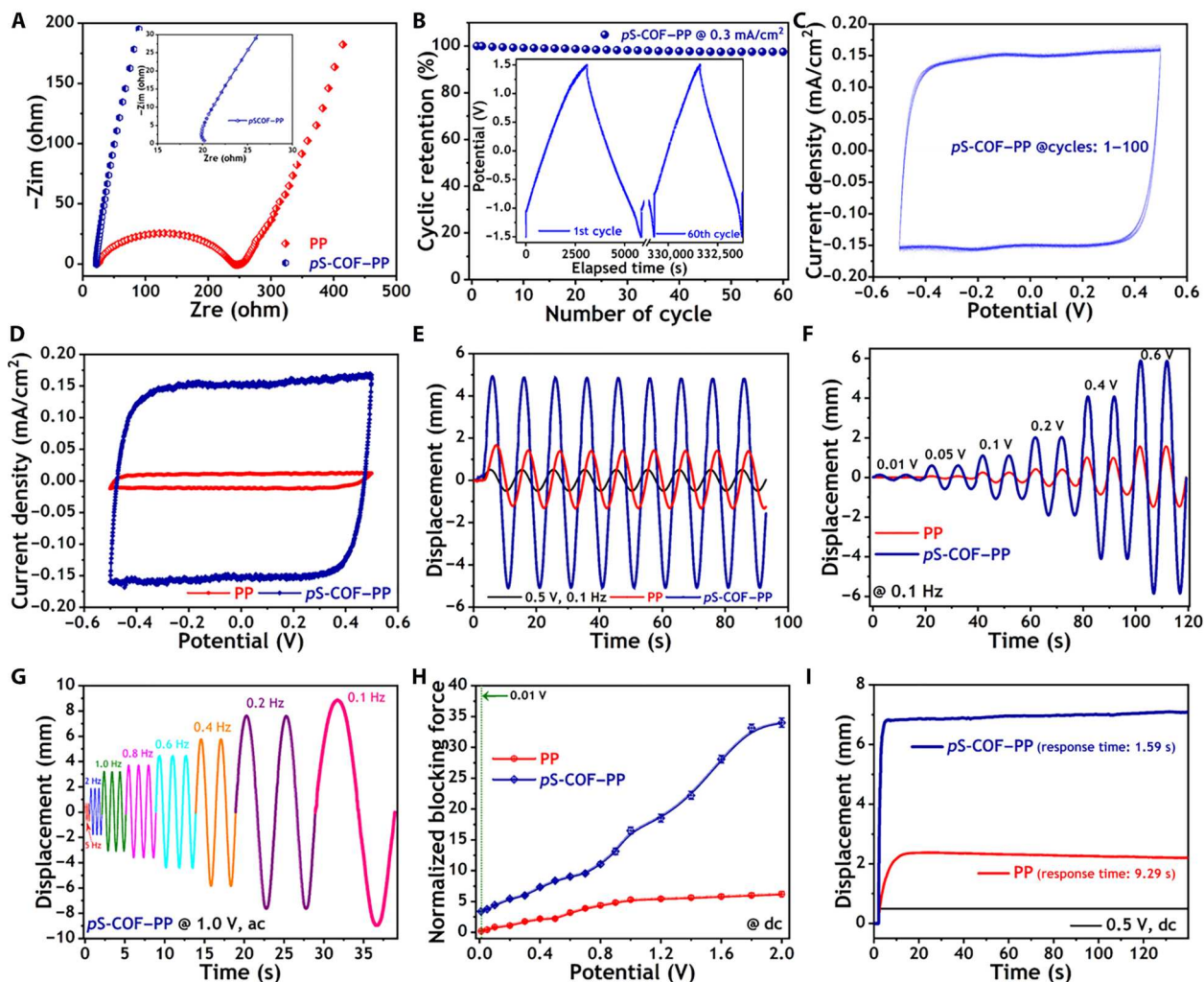

Fig. 4. Methodical electrochemical and actuation performances of common host-triggered *p*S-COFs based soft switch. (**A**) Comparative EIS plots of PEDOT-PSS only (PP) and *p*S-COFs active material (*p*S-COF–PP) based electrochemical soft actuators. Inset: Magnified EIS plot of *p*S-COF–PP. (**B**) Retention of long-term electrochemical cyclic stability for *p*S-COF–PP under an input current density of 0.3 mA cm^{-2}. Inset: Initial and final GCD profiles. (**C**) Stability of electrochemical CV responses for *p*S-COF–PP soft actuator. Typical EDLC-type superimposed response patterns up to 100 cycles under nonstop electrochemical charging/discharging processes are shown. (**D**) Comparative electrochemical CV response patterns for both the PP and *p*S-COF–PP soft actuators. An enhancement of 12-fold areal ionic-capacitance due to the utilization of *p*S-COFs as common electrode-electrolyte host is shown. (**E**) Typical time-dependent contrastive bending response patterns of PP and *p*S-COF–PP electrochemical soft actuators under ±0.5-V sine wave input potential at a constant excitation frequency of 0.1 Hz. (**F**) Comparative electrochemical bending deflections of PP and *p*S-COF–PP soft actuators under the incremental input voltages, starting from near-zero (0.01 V) to ultralow 0.6 V. (**G**) Typical electrochemical bending deflection of *p*S-COF–PP soft actuator under a wide range of excitation frequencies, starting from 0.1 to 5.0 Hz, at a constant sine wave input potential of ±1.0 V. (**H**) Comparative plots of normalized blocking force for PP and *p*S-COF–PP soft actuators under the incremental dc voltages, starting from near-zero (0.01 V) to 2.0 V. (**I**) Comparative time-dependent bending responses of PP and *p*S-COF–PP electrochemical soft actuators at an ultralow 0.5-V dc input potential.

including resistance to acid-base conditions, is crucial when selecting active electrode materials for electrochemical applications, such as electro-ionic soft actuators. To investigate the stability, we immersed the pS-COFs in both the nonaqueous (acetonitrile and chloroform) and aqueous (1 M H_2SO_4 and 1 M KOH) solvents for 20 days. After washing and drying, FTIR analysis [attenuated total reflection (ATR) mode] was performed to understand the effect of these solvents. It was observed that there were no changes in the FTIR peaks when compared to the base pS-COFs materials. The retention of peaks in the FTIR spectra (fig. S7) confirms the stability of pS-COFs in both the aqueous and nonaqueous solvents including acidic and basic solutions.

Electrochemical and actuation performances of pS-COF electrochemical soft actuators

The prepared pS-COF with the aforementioned physicochemical properties has been primarily used as an effective electrode material for the open-air electrochemical ionic actuators, called pS-COF–PP. In a typical soft switch, a solid-state ionic liquid-embedded Nafion membrane is used as a flexible electrolyte, in which mobile $EMIM^+$ cations are electrostatically captured by sulfonated moieties. In contrast, pS-COF was coated onto both surfaces of the electrolyte membrane using PEDOT-PSS as a conductive binder to produce common electrolyte-electrode hosts containing sulfonate moieties to maximize electrochemical performance. These common sulfonate moieties located on both sides of the electrode and electrolyte form relaxing conduction paths for the easy and fast movement of $EMIM^+$ ions. To demonstrate the structural features of the pS-COF–PP soft actuator, we present a schematic with plausible functional moieties in Fig. 1B and fig. S8A. The SEM morphological images display the strongly connected electrolyte-electrode layers and homogeneously distributed pS-COF species on both the surface and cross section of pS-COF–PP (fig. S8, B to E). The presence of pS-COF increases both the charge storage capacity of the electrode interface and the stroking force of the actuator. A reference soft actuator (PP) was fabricated using only PEDOT-PSS as the electrode material to validate our hypothesis of using a common host for the remarkable electrochemical actuation (details of the PP and pS-COF–PP electrochemical actuator fabrication procedures are provided in Materials and Methods). The Nyquist plots of the PP and pS-COF–PP soft actuators were constructed to investigate the improvement in the charge transfer resistance (R_{ct}) and diffusion rate of ions due to the presence of a common electrolyte-electrode host in the solid state (Fig. 4A). It was found that the use of pS-COF as a common sulfonate host notably reduced the R_{ct} value of the PP soft actuator from 250 to 16 ohms and promoted charge transport. The diffusion of electrolyte ions was substantially enhanced in the pS-COF–PP soft actuator, which indirectly confirmed the superiority of the common host platform for maximizing actuation performance (inset of Fig. 4A). The observed increase in the surface electrical conductivity from 147.6 S cm^{-1} (PEDOT-PSS) to 480.1 S cm^{-1} (pS-COF–PEDOT-PSS) strongly correlates with electrochemical impedance spectroscopy (EIS) data (table S3). It can be concluded that pS-COF modulates the PEDOT-PSS electronic structure through ionic interactions and enhances its electron transport properties (34). The facile exchange of guest ions (mainly $EMIM^+$) between the electrode and electrolyte in the pS-COF–PP soft actuator was verified by both the long-term electrochemical cyclic stability and the specific capacitance data (Fig. 4, B and C).

Figure 4B shows the retention of cyclic stability up to 97.6%, even after ~100 hours of continuous charging and discharging cycles conducted at an input current density of 0.3 mA cm^{-2}. The inset in Fig. 4B shows the corresponding initial and final galvanostatic charge-discharge (GCD) profiles. The robust electrochemical stability of the pS-COF–PP soft actuator was further assessed by cyclic voltammetry (CV) (Fig. 4C). The typical EDLC-type CV responses completely overlapped during the first 100 cycles of continuous electrochemical charging and discharging processes. These results strongly support the ability of pS-COF serving as a common electrolyte-electrode host to achieve the maximum electrochemical actuation. Moreover, the electrochemical charge storage capacity of the pS-COFs–PP soft actuator was 12 times higher than that of the similar PP soft actuator (Fig. 4D). The areal capacitance calculated from the CV response of pS-COF–PP was 139 mF cm^{-2}, which was close to that obtained from its GCD profile (137.7 mF cm^{-2}) and 12 times greater than the areal capacitance of the PP actuator (11.5 mF cm^{-2}). The resulting capacitance of the pS-COF–based electrochemical soft actuator was also found to be very high compared to available sulfonated COF-based actuator. This is due to the distinct unit cell structural configuration of pS-COFs, where it contains two times more sulfonated functional groups in comparison to other sulfonated COFs (fig. S11 and table S4). Thus, the common electrolyte-electrode host was mainly responsible for the excellent electrochemical properties of the pS-COF–PP actuator, leading to many advances in the field of electroionic soft actuation (Fig. 4, E to I, and tables S5 and S6). First, at an ultralow sine wave input voltage of 0.5 V, the pS-COF–PP soft actuator [dimensions: 15 mm (active length) by 5 mm (width) by 0.19 mm (thickness)] exhibits a bending deflection of 10 mm, which is almost four times higher than that of the PP actuator with a substantial phase delay reduction of 340% (Fig. 4E). The electrochemical bending signal of the pS-COF–PP soft actuator is observed for the first time at 0.01 V (fig. S9A and Fig. 4F). The common electrolyte-electrode host allows the exchange of electrolyte ions at this near-zero voltage with a peak-to-peak displacement of 0.30 mm, while the threshold limit of other soft actuators is 0.1 V. Figure 4F displays the comparative bending deflection patterns of the PP and pS-COF–PP soft actuators observed at incremental input voltages ranging from 0.01 to 0.6 V, which reflect the suitability of the common host. The fabricated pS-COF also enabled the high-frequency (5.0 Hz) electrochemical actuation of the pS-COF–PP soft actuator at an ultralow input voltage (fig. S9B and Fig. 4G). A substantial bending deflection of 1.56 mm was achieved at 5.0 Hz, which was further enhanced by lowering the oscillation frequency. The common sulfonate-functionalized electrolyte-electrode host also exhibited maximum electrochemical displacements of 3.8, 6.4, 7.6, 9.0, 11.6, 15.2, and 18.3 mm at an input voltage of 1.0 V and excitation frequencies of 2.0, 1.0, 0.8, 0.6, 0.4, 0.2, and 0.1 Hz, respectively (Fig. 4G). The impressive bending deflections at higher frequencies (˃1.0 Hz) observed for the pS-COF–PP soft actuator were mainly attributed to the stress-free fast conduction of electrolyte ions under the ultralow applied potential gradient. Owing to the maximum electrochemical actuation, the bending strain difference (ε) and blocking force (κ) of the pS-COF–PP soft actuator increased notably as compared with literature data (tables S5 and S6 and Fig. 4H). The ε values of the pS-COF–PP soft actuator calculated at ultralow input voltages of 0.5 and 1.0 V and a constant excitation frequency of 0.1 Hz were equal to 0.56 and 0.83%, respectively (table

S5). A previously unattainable blocking force of 0.247 mN was achieved for the *p*S-COF–PP soft actuator at a near-zero applied voltage (0.01 V, dc), which is more than 16 times higher than that of the PP actuator and 3.5 times greater than its own weight. The comparative plots of κ (Fig. 4H) confirm the importance of using *p*S-COFs for producing common host platforms leading to higher actuation forces. They show that the blocking forces of the *p*S-COF–PP soft actuator obtained at working voltages of 0.1, 1.0, and 2.0 V are more than 5, 3, and 6 times higher than that of the PP soft actuator and nearly 5, 14, and 34 times greater than its own weight, respectively. The blocking force of 4.76 mN obtained for the *p*S-COF–PP soft actuator at 2.0 V, dc is the highest value reported up to date (table S6). In addition, the common host triggered a faster relaxing exchange of electrolyte ions, which rapidly increased the actuation speed (Fig. 4I). An instantaneous deflection of 6.85 mm was obtained for the *p*S-COF–PP soft actuator within 1.59 s at an ultralow dc input voltage of 0.5 V and exhibited no back-relaxation, which is a commonly observed phenomenon in the field. Therefore, the *p*S-COF–based common sulfonate host not only overcomes the back-relaxation effect but also increases the actuation speed of the *p*S-COF–PP soft actuator by a factor of 19 as compared with that of the PP actuator. A robust long-cycle durability of *p*S-COF–PP soft actuator up to 60,000 cycles has also been achieved, which can solve the stability problem for open-air robotic applications (fig. S12). Although the maximum electrochemical actuation is actively promoted by the common sulfonate-functionalized electrolyte-electrode host, this study can provide guidelines for developing even stronger electrochemical devices (including soft actuators and energy storage devices) by designing highly capacitive electrode materials.

Demonstration and operation of *p*S-COFs based soft fluidic switch

The superior electrochemical actuation performance of the *p*S-COF–PP actuator at ultralow voltages (Fig. 4) motivated us to construct a soft fluidic switch with a high practical application potential. For this purpose, a *p*S-COF–PP soft actuator acting as a soft switch was installed at the branching point of a Y-shaped fluidic channel consisting of A and B branches with reservoirs attached to their ends (Fig. 5A). The resulting configuration could selectively block either the A or B branch/subchannel with an adequate force upon switching with ultralow electrical stimulation on demand (see Materials and Methods for details). As illustrated in Fig. 5A, two fluids of distinct colors (blue and red) were used to demonstrate the controlled flows in the subchannels (A and B) under dynamic motion. We initially stimulated the *p*S-COF–PP–based soft fluidic switch by applying a voltage of +2.0 V to restrict the flow through subchannel A due to the bending deflection toward the left wall of the main channel with a blocking force of 4.76 mN. This allowed only the flow of the red-colored fluid through subchannel B toward the reservoir (Fig. 5B). Afterwards, by switching the input electrical stimulation from +2.0 to −2.0 V, the soft switch was actuated to the opposite direction and blocked subchannel B (the right wall of the main channel) while opening the A subchannel for the fluid flow (Fig. 5C). The blue fluid subsequently flowed through subchannel A and was stored in the reservoir at the end of the experiment (Fig. 5D). Movie S1 illustrates the operation of the proposed fluidic switch in real time and its working mechanism. Therefore, the soft fluidic switch can selectively block subchannel A or B by switching the input stimulation from a positive to negative

voltage or vice versa to allow the flow of a preferred fluid to a certain reservoir. This successful demonstration with the *p*S-COF–PP soft actuator can certainly broaden the application areas of electroactive soft robots and may attract strong interest in droplet-based microfluidics (*35*–*38*). In addition, this switch can be potentially implemented in certain biomedical applications, such as a lab-on-a-chip, which requires autonomous manipulation of fluidic samples. The manipulation of blood cells in the blood vessels of an animal (including the human body) is another possible application of the switch owing to its soft nature. The most challenging issue of designing mechanical systems for vascular systems is the formation of blood clots due to the collision of blood cells with hard mechanical components. Therefore, the use of soft fluidic switches can decrease the risk of blood clots in vascular systems as compared with that of conventional hard components.

DISCUSSION

In this study, we report the *p*S-COF–PP soft actuator introducing a unique concept of a common electrolyte-electrode host as a distinctively tunable platform for maximizing electrochemical actuation. By using the sulfonate functional group as a common host for $EMIM^+$ cations, the specific charge capacitance of the PP soft actuator was increased by a factor of 12 from 11.5 to 139 mF cm^{-2}, while the electrochemical R_{ct} value was decreased from 250 to 16 ohms. The *p*S-COF provides a relaxing and stress-free electrochemical transportation path for $EMIM^+$ ions between the electrode and electrolyte to achieve a remarkable high-frequency bending deflection and record-high bending strain of 0.83% at an ultralow input voltage of 1.0 V. The blocking force of 4.76 mN was obtained for the *p*S-COF–PP soft actuator at 2.0 V. Last, the excellent electrochemical actuation properties of the *p*S-COF–PP actuator used as a soft fluidic switch confirmed the importance of using a common electrolyte-electrode host. We anticipate that common-host engineering using nanoporous and electronically conjugated high-capacitive active electrode materials will become a general strategy for maximizing the electrochemical actuation performance and developing high-performance energy-storage devices with a wide range of practical applications.

MATERIALS AND METHODS
Chemicals and materials
DSA, phloroglucinol, magnesium sulfate (anhydrous, 99.5%), trifluoroacetic acid (99%), hydrochloric acid (37%), N,N′-dimethylformamide (DMF; anhydrous, 99.8%), N,N-dimethylacetamide (DAMc), methyl alcohol (MeOH, 99.9%), dimethyl sulfoxide (99.7%), deuterochloroform (99.8 atom% D), acetone (99.5%), and Nafion were purchased from Sigma-Aldrich, USA. The ionic liquid consisting of EMIM tetrafluoroborate (EMIM-BF$_4$, 98%) was obtained from IOLITEC GmbH. PEDOT-PSS was purchased from Heraeus in the form of the CLEVIOS PH 1000 dispersion.

Synthesis of *p*S-COF
Initially, TP of sufficient purity was synthesized as described elsewhere (*39*). Recently, TP has shown strong potential in developing various functional COFs for advanced engineering applications (*40*–*44*). Afterwards, four glass ampoules were filled with the as-synthesized TP (100 mg, 0.48 mmol), DSA (266 mg, 0.72 mmol),
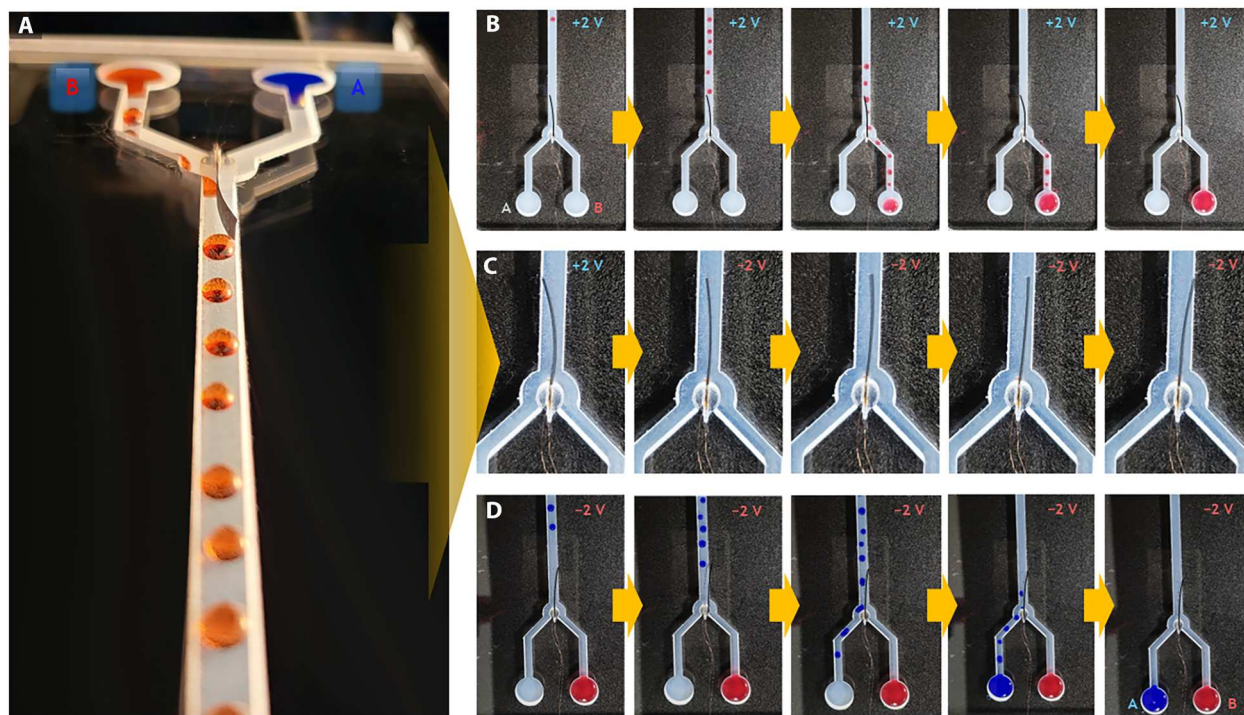
Fig. 5. Realization of the *p*S-COF−PP electrochemical soft fluidic switch to control the fluid flow under dynamic motion. (**A**) Overall setup, which contains a Y-shape fluidic channel, electrochemical soft actuator that is installed at the branching point, A and B subchannels with reservoirs at the end, and solutions with two different colors, blue and red. (**B**) Activating the soft fluidic switch by +2.0-V stimulation to restrict the flow of fluid through the subchannel A. Red color fluid droplets were only flowed through subchannel B and stored in the reservoir at the end. (**C**) Switching the stimulation from +2.0 to −2.0 V for the movement of the actuator to the opposite end at the fluidic channel. (**D**) Blocking of subchannel B by the soft switch in response to −2.0-V stimulation and allow to flow the fluid through subchannel A. Blue color fluid droplets were flowed through subchannel A and lastly stored in the reservoir at the end. Movie S1 was provided for real-time realization of the proposed demonstration with working mechanism.

DMF (4 ml), and MeOH (5 ml) each. The filled ampoules were ultrasonicated for 20 min to obtain a homogeneous dispersion and subsequently degassed by performing up to five freeze-pump-thaw cycles before flame sealing. The degassed and sealed ampoules were transferred to an electrical oven to promote the solvothermal formation of imide linkages between TA and DSA at a temperature of 120°C for 72 hours. The light-yellow dispersion changed to a dark-brown *p*S-COF precipitate after the solvothermal treatment. This precipitate was collected by filtration followed by successive washing with DMF (200 ml), MeOH (100 ml), and acetone. Last, the resultant *p*S-COF was purified by Soxhlet extraction using a mixture of DMF/acetone solvents (3:2 V/v, 48 hours). The optimization for the synthetic procedure of *p*S-COF was done by screening various possible solvent mixtures. After a judicious solvent screening (table S7), the optimized *p*S-COF with the highest porosity is obtained using DMF and methanol solvent mixture in the ratio of 4:5.

Fabrication of the *p*S-COF−based electrochemical soft actuator

The fabrication method described earlier (*16*, *20*, *31*, *34*) was followed to obtain the pS-COF−PP actuator. In this process, an electrolyte membrane [ionic liquid (EMIM-BF$_4$)−embedded Nafion; thickness, 110 μm] was initially prepared by solution casting. EMIM-BF$_4$ (30 mg/ml) containing a homogeneous Nafion solution (50 mg/ml in DAMc) was cast onto a flat glass petri dish (diameter,

5 cm) and dried in a vacuum oven at 85°C for 7 hours. Afterwards, the homogeneous dispersion of *p*S-COF [1 ml, dimethyl sulfoxide (DMSO); sonication, 10 min] was mixed with the aqueous solution of PEDOT-PSS (0.45 mg/ml), and the resultant electrode ink was stirred for 24 hours at 25°C. An equal volume of the as-prepared electrode ink was drop cast onto the surfaces of the electrolyte membrane (one after another) followed by the complete evaporation of the solvent at 70°C for 1 hour. The *p*S-COF loading in the electrode ink was optimized by evaluating the electrochemical actuation performance of the corresponding soft actuators (fig. S10). Figure S10 (A and B) shows the electrochemical actuation performance of the *p*S-COF−PP soft actuator with several wt % of *p*S-COF loading. The optimized *p*S-COF−PP soft actuator (thickness, 180 μm) was cut into a piece with a total length of 20 mm and width of 4 mm for electrochemical analysis. To evaluate the efficacy of *p*S-COF as a common host platform, a pristine PEDOT-PSS-based electrochemical soft actuator (PP) with the same dimensions was fabricated via the abovementioned procedure. It is worth noting that the same amount of DMSO was used in the preparation of the PEDOT-PSS electrode ink.

Superhydrophobic coating on to the surface of *p*S-COF−PP soft actuator

For the use of proposed *p*S-COF−PP actuator in electrochemical soft fluidic switch, both surfaces were initially coated by a commercially available superhydrophobic coating one by one. It is a very simple

two-step spray coating process where the base coat is applied on to the electrode surface in step 1 followed by top coat in step 2. Both coating processes were applied for a second only after the surface was naturally dried. The real-time optical image for coated and uncoated surface of pS-COF–PP was shown in fig. S3A, while wetting nature of the water droplet on to the bare and coated surface of pS-COF–PP soft actuator was pictorially shown in fig. S3 (B and C, respectively). It was observed that after superhydrophobic coating treatment, the water contact angle of the surface enhanced enormously. Movie S2 shows how water droplets escape when they come in contact with the surface of a coated electrode (here pS-COF–PP soft actuator). Movie S1 shows how the superhydrophobic surface of pS-COF–PP based soft fluidic switch restricts the adhesion of fluid droplets under dynamic motion. The corresponding changes in surface morphology before and after coating for the pS-COF–PP soft actuator are shown in fig. S3 (D and E, respectively). The formation of nanoscale surface morphologies and micro/nanostructured particles were visualized because of the applied coating. Such micro/nanostructure substantially increased the surface roughness of the electrodes and improved their hydrophobicity. The thin and light hydrophobic coating layer does not change the actual electrochemical actuation performance of the pS-COF–PP soft actuator as shown in table S8. To evaluate the efficacy of proposed electrochemical soft switch toward controlling the fluid flow in a confined fluidic channel under dynamic motion, a Y-shape narrow channel was fabricated by cutting 10-mm-thick acrylic plate using laser cutter (fig. S3F). The optical image of proposed pS-COF based electrochemical soft fluidic switch is shown in fig. S3G. As shown in fig. S3H, the soft fluidic switch was installed at the branching point of Y-shape channel so that upon electrochemical actuation it can selectively block either A or B subchannel and allow to flow the fluid in one direction only (movie S1).

Material characterization

The pS-COF structure was examined by various advanced scientific characterization techniques. The nanoporous surface images of pS-COF were obtained by FESEM and HRTEM using a Hitachi-SU8230 scanning electron microscope and Titan Double Cs-corrected transmission electron microscope (Titan cubed G2 60-300, FEI) instrument, respectively. The elemental mapping images was obtained at the nanometer scale using the scanning transmission electron microscope instrument equipped with a HAADF module. The building-block elements and their atomic percentages were evaluated by a Thermo Fisher Scientific FlashSmart elemental analyzer (CHNS-O). The formation of imine linkages and available polar chemical bonds of pS-COF were assessed from the FTIR spectra recorded on a Thermo Fisher Scientific spectrometer (Nicolet iS50) using KBr pellets. The UV and visible light absorption properties of pS-COF were analyzed by recording solid-state UV-visible diffuse reflectance spectra on a UV-visible/near-infrared spectrometer (PerkinElmer, Lambda 1050). The chemically nonequivalent protons and carbons of pS-COF were detected by solid-state ^{1}H and ^{13}C CP-MAS NMR using a 400-MHz NMR spectrometer (Agilent 400-MHz 54-mm NMR DD2). The existence of crystalline phases in pS-COF was confirmed using a high-resolution powder x-ray diffractometer (SmartLab, Rigaku) with Cu-Kα serving as the radiation source (λ = 1.54 Å) and SAXS instrument (NANOPIX, Rigaku). The nanoporous structural surface of pS-COF was examined by recording nitrogen (N_2) physisorption

isotherms at 77 K using a Micromeritics surface area and pore size analyzer (3Flex). The resultant adsorption-desorption isotherms were evaluated to obtain the pore parameters, including the Brunauer-Emmett-Teller specific surface area, pore size, and pore volume. Before analysis, the sample was degassed at 150°C for 12 hours under vacuum, and all N_2 adsorption-desorption measurements were conducted thrice to ensure reproducibility. Possible atomic configurations in the pS-COF structure were identified by analyzing the XPS profiles obtained using a Thermo VG Scientific instrument (K-alpha) at a base pressure of 3×10^{-8} Pa. The thermal stability of pS-COF was evaluated by recording thermogravimetric analysis (TGA) curves using a high-resolution NETZSCH-TG 209F1 Libra TGA instrument. In this process, the sample was heated to 1000°C under a N_2 atmosphere at a heating rate of 10°C/min. The surface electrical conductivities of the pS-COF–based (pS-COF–PEDOT-PSS) and PEDOT-PSS electrode layers (thickness, 30 ± 5.0 μm) were measured by a standard four-probe measurement device (MSTECH, Model:4000) connected to a Keithley SourceMeter 2400 instrument.

Electrochemical characterization

The electrochemical charge storage capacities, ion diffusions, and R_{ct} values of the PP and pS-COF–PP soft actuators were extracted from the CV and EIS data obtained using an electrochemical workstation (VersaStat3, Princeton Applied Research). Both the CV and EIS measurements were performed in a two-electrode configuration, and the frequency was selected in the region between 0.01 and 500,000 Hz at an amplitude of 50-mV RMS (45).

The areal specific capacitances of the PP and pS-COF–PP electrochemical soft actuators were calculated via the following equation

$$C_{sp} = \frac{A}{2 \times \Delta V \times v \times S} \tag{1}$$

where A is the area inside the CV response curve, ΔV is the working potential window, v is the scan rate, and S is the active electrode area.

The electrochemical actuation characteristics of the PP and pS-COF–PP soft actuators were determined by applying ultralow input voltages ($\leq$1.0 V) with different amplitudes and excitation frequencies. To record the real-time bending deflections of the soft actuators, a laser displacement sensor (Keyence, LK031) was used (34, 45, 46).

The blocking forces (κ) of the electrochemical soft actuators were measured using an LVS-5GA load cell (Kyowa) as a force sensor with a capacity of 50 mN (47).

The ultralow voltage bending strain difference (ε) between the two opposite electrode layers in the pS-COF–PP soft actuator was calculated as follows (31)

$$\varepsilon = \frac{2\delta d}{l^2 + \delta^2} \tag{2}$$

where δ is the maximum deflection from the original position of the soft actuator, d is the actuator thickness, and l is the active actuation length.

Supplementary Materials

This PDF file includes:

Figs. S1 to S12

Tables S1 to S8
Legends for movies S1 and S2
References

Other Supplementary Material for this manuscript includes the following:
Movies S1 and S2

REFERENCES AND NOTES

1. P. Simon, Y. Gogotsi, Materials for electrochemical capacitors. *Nat. Mater.* **7**, 845–854 (2008).

2. Y. Yu, K. Zhang, H. Parks, M. Babar, S. Carr, I. M. Craig, M. Van Winkle, A. Lyssenko, T. Taniguchi, K. Watanabe, V. Viswanathan, D. K. Bediako, Tunable angle-dependent electrochemistry at twisted bilayer graphene with moiré flat bands. *Nat. Chem.* **14**, 267–273 (2022).

3. X. Lang, A. Hirata, T. Fujita, M. Chen, Nanoporous metal/oxide hybrid electrodes for electrochemical supercapacitors. *Nat. Nanotechnol.* **6**, 232–236 (2011).

4. C. Choi, D. S. Ashby, D. M. Butts, R. H. DeBlock, Q. Wei, J. Lau, B. Dunn, Achieving high energy density and high power density with pseudocapacitive materials. *Nat. Rev. Mater.* **5**, 5–19 (2020).

5. T. Lin, I. W. Chen, F. Liu, C. Yang, H. Bi, F. Xu, F. Huang, Nitrogen-doped mesoporous carbon of extraordinary capacitance for electrochemical energy storage. *Science* **350**, 1508–1513 (2015).

6. D. N. Futaba, K. Hata, T. Yamada, T. Hiraoka, Y. Hayamizu, Y. Kakudate, O. Tanaike, H. Hatori, M. Yumura, S. Iijima, Shape-engineerable and highly densely packed single-walled carbon nanotubes and their application as super-capacitor electrodes. *Nat. Mater.* **5**, 987–994 (2006).

7. P. Simon, Y. Gogotsi, Perspectives for electrochemical capacitors and related devices. *Nat. Mater.* **19**, 1151–1163 (2020).

8. X. Wang, M. Salari, D. E. Jiang, J. Chapman Varela, B. Anasori, D. J. Wesolowski, S. Dai, M. W. Grinstaff, Y. Gogotsi, Electrode material–ionic liquid coupling for electrochemical energy storage. *Nat. Rev. Mater.* **5**, 787–808 (2020).

9. S. Fleischmann, Y. Zhang, X. Wang, P. T. Cummings, J. Wu, P. Simon, Y. Gogotsi, V. Presser, V. Augustyn, Continuous transition from double-layer to Faradaic charge storage in confined electrolytes. *Nat. Energy* **7**, 222–228 (2022).

10. H. Sun, J. Zhu, D. Baumann, L. Peng, Y. Xu, I. Shakir, Y. Huang, X. Duan, Hierarchical 3D electrodes for electrochemical energy storage. *Nat. Rev. Mater.* **4**, 45–60 (2019).

11. G. Gu, M. Schmid, P. W. Chiu, A. Minett, J. Fraysse, G. T. Kim, S. Roth, M. Kozlov, E. Muñoz, R. H. Baughman, V$_2$O$_5$ nanofibre sheet actuators. *Nat. Mater.* **2**, 316–319 (2003).

12. O. Kim, H. Kim, U. H. Choi, M. J. Park, One-volt-driven superfast polymer actuators based on single-ion conductors. *Nat. Commun.* **7**, 13576 (2016).

13. F. Yu, J. H. Ciou, S. Chen, W. C. Poh, J. Chen, J. Chen, K. Haruethai, J. Lv, D. Gao, P. S. Lee, Ionic covalent organic framework based electrolyte for fast-response ultra-low voltage electrochemical actuators. *Nat. Commun.* **13**, 390 (2022).

14. C. Lu, Y. Yang, J. Wang, R. Fu, X. Zhao, L. Zhao, Y. Ming, Y. Hu, H. Lin, X. Tao, Y. Li, W. Chen, High-performance graphdiyne-based electrochemical actuators. *Nat. Commun.* **9**, 752 (2018).

15. O. Kim, T. J. Shin, M. J. Park, Fast low-voltage electroactive actuators using nanostructured polymer electrolytes. *Nat. Commun.* **4**, 2208 (2013).

16. M. Mahato, R. Tabassian, V. H. Nguyen, S. Oh, S. Nam, W. J. Hwang, I. K. Oh, CTF-based soft touch actuator for playing electronic piano. *Nat. Commun.* **11**, 5358 (2020).

17. G. Wu, Y. Hu, Y. Liu, J. Zhao, X. Chen, V. Whoehling, C. Plesse, G. T. Nguyen, F. Vidal, W. Chen, Graphitic carbon nitride nanosheet electrode-based high-performance ionic actuator. *Nat. Commun.* **6**, 7258 (2015).

18. X. Yu, H. Cheng, M. Zhang, Y. Zhao, L. Qu, G. Shi, Graphene-based smart materials. *Nat. Rev. Mater.* **2**, 17046 (2017).

19. W. Lu, A. G. Fadeev, B. Qi, E. Smela, B. R. Mattes, J. Ding, G. M. Spinks, J. Mazurkiewicz, D. Zhou, G. G. Wallace, D. R. MacFarlane, Use of ionic liquids for π-conjugated polymer electrochemical devices. *Science* **297**, 983–987 (2002).

20. M. Kotal, J. Kim, K. J. Kim, I. K. Oh, Sulfur and nitrogen co-doped graphene electrodes for high-performance ionic artificial muscles. *Adv. Mater.* **28**, 1610–1615 (2016).

21. S. Bi, H. Banda, M. Chen, L. Niu, M. Chen, T. Wu, J. Wang, R. Wang, J. Feng, T. Chen, M. Dincă, Molecular understanding of charge storage and charging dynamics in supercapacitors with MOF electrodes and ionic liquid electrolytes. *Nat. Mater.* **19**, 552–558 (2020).

22. M. Mahato, S. Nam, R. Tabassian, S. Oh, V. H. Nguyen, I. K. Oh, Electronically conjugated multifunctional covalent triazine framework for unprecedented CO$_2$ selectivity and high-power flexible supercapacitor. *Adv. Funct. Mater.* **32**, 2107442 (2022).

23. D. Feng, T. Lei, M. R. Lukatskaya, J. Park, Z. Huang, M. Lee, L. Shaw, S. Chen, A. A. Yakovenko, A. Kulkarni, J. Xiao, Robust and conductive two-dimensional metal–organic frameworks with exceptionally high volumetric and areal capacitance. *Nat. Energy* **3**, 30–36 (2018).

24. N. Huang, P. Wang, D. Jiang, Covalent organic frameworks: a materials platform for structural and functional designs. *Nat. Rev. Mater.* **1**, 16068 (2016).

25. K. T. Tan, S. Ghosh, Z. Wang, F. Wen, D. Rodríguez-San-Miguel, J. Feng, N. Huang, W. Wang, F. Zamora, X. Feng, A. Thomas, Covalent organic frameworks. *Nat. Rev. Methods Primers* **3**, 1–19 (2023).

26. L. Cao, I. C. Chen, Z. Li, X. Liu, M. Mubashir, R. A. Nuaimi, Z. Lai, Switchable Na+ and K+ selectivity in an amino acid functionalized 2D covalent organic framework membrane. *Nat. Commun.* **13**, 7894 (2022).

27. G. Wang, N. Chandrasekhar, B. P. Biswal, D. Becker, S. Paasch, E. Brunner, M. Addicoat, M. Yu, R. Berger, X. Feng, A crystalline, 2D polyarylimide cathode for ultrastable and ultrafast Li storage. *Adv. Mater.* **31**, e1901478 (2019).

28. D. Guo, D. B. Shinde, W. Shin, E. Abou-Hamad, A. H. Emwas, Z. Lai, A. Manthiram, Foldable solid-state batteries enabled by electrolyte mediation in covalent organic frameworks. *Adv. Mater.* **34**, e2201410 (2022).

29. K. Jeong, S. Park, G. Y. Jung, S. H. Kim, Y. H. Lee, S. K. Kwak, S. Y. Lee, Solvent-free, single lithium-ion conducting covalent organic frameworks. *J. Am. Chem. Soc.* **141**, 5880–5885 (2019).

30. S. Park, I. Kristanto, G. Y. Jung, D. B. Ahn, K. Jeong, S. K. Kwak, S. Y. Lee, A single-ion conducting covalent organic framework for aqueous rechargeable Zn-ion batteries. *Chem. Sci.* **11**, 11692–11698 (2020).

31. M. Mahato, R. Tabassian, V. H. Nguyen, S. Oh, S. Nam, K. J. Kim, I. K. Oh, Sulfur-and nitrogen-rich porous π-conjugated COFs as stable electrode materials for electro-ionic soft actuators. *Adv. Funct. Mater.* **30**, 1–8 (2020).

32. X. Chen, M. Addicoat, E. Jin, L. Zhai, H. Xu, N. Huang, Z. Guo, L. Liu, S. Irle, D. Jiang, Locking covalent organic frameworks with hydrogen bonds: general and remarkable effects on crystalline structure, physical properties, and photochemical activity. *J. Am. Chem. Soc.* **137**, 3241–3247 (2015).

33. S. Kandambeth, D. B. Shinde, M. K. Panda, B. Lukose, T. Heine, R. Banerjee, Enhancement of chemical stability and crystallinity in porphyrin-containing covalent organic frameworks by intramolecular hydrogen bonds. *Angew. Chem.Int. Ed. Engl.* **52**, 13052–13056 (2013).

34. S. Umrao, R. Tabassian, J. Kim, V. H. Nguyen, Q. Zhou, S. Nam, I. K. Oh, MXene artificial muscles based on ionically cross-linked Ti3C2Txelectrode for kinetic soft *robotics. Sci. Robot.* **4**, eaaw7797 (2019).

35. H. D. Xi, H. Zheng, W. Guo, A. M. Gañán-Calvo, Y. Ai, C. W. Tsao, J. Zhou, W. Li, Y. Huang, N. T. Nguyen, S. H. Tan, Active droplet sorting in microfluidics: A review. *Lab Chip* **17**, 751–771 (2017).

36. D. P. Regan, C. Howell, Droplet manipulation with bioinspired liquid-infused surfaces: A review of recent progress and potential for integrated detection. *Curr. Opin. Colloid Interface Sci.* **39**, 137–147 (2019).

37. J. H. Kim, S. M. Kang, B. J. Lee, H. Ko, W. G. Bae, K. Y. Suh, M. K. Kwak, H. E. Jeong, Remote manipulation of droplets on a flexible magnetically responsive film. *Sci. Rep.* **5**, 17843 (2015).

38. D. Paulssen, S. Hardt, P. A. Levkin, Droplet sorting and manipulation on patterned two-phase slippery lubricant-infused surface. *ACS Appl. Mater. Interfaces* **11**, 16130–16138 (2019).

39. J. H. Chong, M. Sauer, B. O. Patrick, M. J. MacLachlan, Highly stable keto-enamine salicylideneanilines. *Org. Lett.* **5**, 3823–3826 (2003).

40. S. Chandra, T. Kundu, K. Dey, M. Addicoat, T. Heine, R. Banerjee, Interplaying intrinsic and extrinsic proton conductivities in covalent organic frameworks. *Chem. Mater.* **28**, 1489–1494 (2016).

41. B. P. Biswal, S. Chandra, S. Kandambeth, B. Lukose, T. Heine, R. Banerjee, Mechanochemical synthesis of chemically stable isoreticular covalent organic frameworks. *J. Am. Chem. Soc.* **135**, 5328–5331 (2013).

42. S. Kandambeth, A. Mallick, B. Lukose, M. V. Mane, T. Heine, R. Banerjee, Construction of crystalline 2D covalent organic frameworks with remarkable chemical (acid/base) stability via a combined reversible and irreversible route. *J. Am. Chem. Soc.* **134**, 19524–19527 (2012).

43. S. Bag, H. S. Sasmal, S. P. Chaudhary, K. Dey, D. Blätte, R. Guntermann, Y. Zhang, M. Položij, A. Kuc, A. Shelke, R. K. Vijayaraghavan, T. G. Ajithkumar, S. Bhattacharyya, T. Heine, T. Bein, R. Banerjee, covalent organic framework thin-film photodetectors from solution-processable porous nanospheres. *J. Am. Chem. Soc.* **145**, 1649–1659 (2023).

44. H. S. Sasmal, A. Kumar Mahato, P. Majumder, R. Banerjee, Landscaping covalent organic framework nanomorphologies. *J. Am. Chem. Soc.* **144**, 11482–11498 (2022).

45. M. Mahato, W. J. Hwang, R. Tabassian, S. Oh, V. H. Nguyen, S. Nam, J. S. Kim, H. Yoo, A. K. Taseer, M. J. Lee, H. Zhang, I. K. Oh, A Dual-Responsive Magnetoactive and Electro–

Ionic Soft Actuator Derived from a Nickel-Based Metal–Organic Framework. *Adv. Mater.* **34**, e2203613 (2022).

46. M. Garai, M. Mahato, S. Nam, E. Kim, D. Seo, Y. Lee, V. H. Nguyen, S. Oh, P. Sambyal, H. Yoo, A. K. Taseer, I. K. Oh, Metal Organic Framework-MXene Nanoarchitecture for Fast Responsive and Ultra-Stable Electro-Ionic Artificial Muscles. *Adv. Funct. Mater.* **33**, 2212252 (2023).

47. R. Tabassian, M. Mahato, S. Nam, V. H. Nguyen, A. Rajabi-Abhari, I. K. Oh, Electro-active and photo-active vanadium oxide nanowire thermo-hygroscopic actuators for kirigami pop-up. *Adv. Sci. (Weinh)* **8**, e2102064 (2021).

48. M. T. Manzoor, V. H. Nguyen, S. Umrao, J. H. Kim, R. Tabassian, J. E. Kim, I. K. Oh, Mutually exclusive p-type and n-type hybrid electrode of MoS2 and MoS2 and graphene for artificial soft touch fingers. *Adv. Funct. Mater.* **29**, 1905454 (2019).

49. S. Roy, J. Kim, M. Kotal, R. Tabassian, K. J. Kim, I. K. Oh, Collectively exhaustive electrodes based on covalent organic framework and antagonistic Co-doping for electroactive ionic artificial muscles. *Adv. Funct. Mater.* **29**, 1900161 (2019).

50. M. Kotal, R. Tabassian, S. Oh, I. K. Oh, Metal–organic framework-derived graphitic nanoribbons anchored on graphene for electroionic artificial muscles. *Adv. Funct. Mater.* **30**, 1910326 (2020).

51. G. Wu, Y. Hu, J. Zhao, T. Lan, D. Wang, Y. Liu, W. Chen, Ordered and active nanochannel electrode design for high-performance electrochemical actuator. *Small* **12**, 4986–4992 (2016).

52. G. Wu, X. Wu, Y. Xu, H. Cheng, J. Meng, Q. Yu, X. Shi, K. Zhang, W. Chen, S. Chen, High-performance hierarchical black-phosphorous-based soft electrochemical actuators in bioinspired applications. *Adv. Mater.* **31**, e1806492 (2019).

53. D. Wang, C. Lu, J. Zhao, S. Han, M. Wu, W. Chen, High energy conversion efficiency conducting polymer actuators based on PEDOT: PSS/MWCNTs composite electrode. *RSC Adv.* **7**, 31264–31271 (2017).

54. N. Terasawa, K. Asaka, Electrochemical and electromechanical properties of activated multi-walled carbon nanotube polymer actuator that surpass the performance of a single-walled carbon nanotube polymer actuator. *Mater. Today: Proc.* **3**, S178–S183 (2016).

55. T. Fukushima, K. Asaka, A. Kosaka, T. Aida, Fully plastic actuator through layer-by-layer casting with ionic-liquid-based bucky gel. *Angew. Chem. Int. Ed. Engl.* **44**, 2410–2413 (2005).

56. J. Torop, V. Palmre, M. Arulepp, T. Sugino, K. Asaka, A. Aabloo, Flexible supercapacitor-like actuator with carbide-derived carbon electrodes. *Carbon* **49**, 3113–3119 (2011).

57. R. K. Cheedarala, J. H. Jeon, C. D. Kee, I. K. Oh, Bio-inspired all-organic soft actuator based on a π–π stacked 3D ionic network membrane and ultra-fast solution processing. *Adv. Funct. Mater.* **24**, 6005–6015 (2014).

58. V. H. Nguyen, J. Kim, R. Tabassian, M. Kotal, K. Jun, J.-H. Oh, J.-M. Son, M. T. Manzoor, K. J. Kim, I.-K. Oh, Electroactive Artificial Muscles Based on Functionally Antagonistic Core–Shell Polymer Electrolyte Derived from PS-b-PSS Block Copolymer. *Adv. Sci.* **6**, 1801196 (2018).

59. J. Kim, J. H. Jeon, H. J. Kim, H. Lim, I. K. Oh, Durable and water-floatable ionic polymer actuator with hydrophobic and asymmetrically laser-scribed reduced graphene oxide paper electrodes. *ACS Nano* **8**, 2986–2997 (2014).

60. S. S. Kim, J. H. Jeon, H. I. Kim, C. D. Kee, I. K. Oh, High-fidelity bioelectronic muscular actuator based on graphene-mediated and TEMPO-oxidized bacterial cellulose. *Adv. Funct. Mater.* **25**, 3560–3570 (2015).

61. L. Lu, W. Chen, Biocompatible composite actuator: a supramolecular structure consisting of the biopolymer chitosan, carbon nanotubes, and an ionic liquid. *Adv. Mater.* **22**, 3745–3748 (2010).

62. L. Lu, J. Liu, Y. Hu, Y. Zhang, H. Randriamahazaka, W. Chen, Highly stable air working bimorph actuator based on a graphene nanosheet/carbon nanotube hybrid electrode. *Adv. Mater.* **24**, 4317–4321 (2012).

63. R. Tabassian, J. Kim, V. H. Nguyen, M. Kotal, I. K. Oh, Functionally Antagonistic hybrid electrode with hollow tubular graphene mesh and nitrogen-doped crumpled graphene for high-performance ionic soft actuators. *Adv. Funct. Mater.* **28**, 1705714 (2018).

64. M. Kotal, J. Kim, R. Tabassian, S. Roy, V. H. Nguyen, N. Koratkar, I. K. Oh, Highly Bendable Ionic Soft Actuator Based on Nitrogen-Enriched 3D Hetero-Nanostructure Electrode. *Adv. Funct. Mater.* **28**, 1802464 (2018).

65. J. Kim, S. H. Bae, M. Kotal, T. Stalbaum, K. J. Kim, I. K. Oh, Soft but powerful artificial muscles based on 3D graphene–CNT–Ni heteronanostructures. *Small* **13**, 1701314 (2017).

66. S. Liu, Y. Liu, H. Cebeci, R. G. D. Villoria, J. H. Lin, B. L. Wardle, Q. M. Zhang, High electromechanical response of ionic polymer actuators with controlled-morphology aligned carbon nanotube/nafion nanocomposite electrodes. *Adv. Funct. Mater.* **20**, 3266–3271 (2010).

67. M. Biso, A. Ansaldo, D. N. Futaba, K. Hata, D. Ricci, Cross-linking super-growth carbon nanotubes to boost the performance of bucky gel actuators. *Carbon* **49**, 2253–2257 (2011).

68. V. Palmre, D. Brandell, U. Maeorg, J. Torop, O. Volobujeva, A. Punning, U. Johanson, M. Kruusmaa, A. Aabloo, Nanoporous carbon-based electrodes for high strain ionomeric bending actuators. *Smart Mater. Struct.* **18**, 095028 (2009).